MAGNETIC BEARING ACTUATOR DESIGN FOR A GAS EXPANDER GENERATOR

Alexei V. Filatov, Patrick T. McMullen, Lawrence A. Hawkins, and Eric J. Blumber
CALNETIX, 12880 Moore Street, Cerritos, CA, 90703
afilatov@calnetix.com

ABSTRACT

A magnetic bearing system for a high-speed cryogenic gas expander/generator is presented. The expander represents a new class of such devices that, in contrast to the earlier technologies, converts the expanding gas energy into electrical power using a direct drive generator. The magnetic bearing and generator constitute a functionally complete unit that can be used in a variety of applications utilizing different expander wheels and operating at various speeds.

In order to obtain a compact design and increase rotor first bending frequency, the axial magnetic bearing is designed to have different pole areas on different sides of the thrust disk. This results in different load capacities in different directions, matching operational conditions of the unit. Regardless this anisotropy, the bearing features linear force vs current dependence.

Radial and angular suspension of the rotor is achieved using two patented homopolar PM-biased radial bearings. The paper discusses design and analysis of these bearings. In spite of the three-dimensional nature of the electromagnetic problem, combination of analytical solution and 2D FEA was found to be an adequate tool for the bearing analysis.

Theoretical predictions of the bearing performance have been found to be in a good agreement with experimental data.

INTRODUCTION

Gas expanders are used to extract pure gases such as nitrogen, oxygen, and argon from the ambient air utilizing the difference in the gas condensation temperatures (cryogenic distillation). During the distillation process, pressurized gas spins an impeller mounted on a shaft connected to some device that produces drag torque, thus limiting the shaft speed and dissipating energy being released during the gas expansion. Conventionally, for power levels below 100 kW, this energy was dissipated in oil-loading units or atmospheric blowers, and the shaft was supported by oil bearings. For higher power levels, the energy was dissipated by driving a low speed generator through a gearbox. The new generation of the gas expanders features permanent magnet direct-drive electrical generator and magnetic bearings. The generator converts the gas energy into electricity for supply to the electrical grid. Using magnetic bearings makes the system completely "oil-free", thus simplifying its design and eliminating problems associated with using oil in cryogenic equipment and risks of accidental contamination of the process products.

The design goal was to develop a universal generator/bearing module that could be used in a variety of gas expanders utilizing different expander wheels ranging in weight from 0.16 kg (0.35 lb) to 2.3 kg (5.1 lb) and operating at various speeds from 9,000 to 30,000 RPM. Additionally, all configurations needed to operate below the first bending mode of the rotor. This requirement was somewhat difficult because a fairly large thrust rotor was needed to accommodate the axial design load required for the largest expander wheel (up to 1750 lbf towards the impeller). This paper describes the magnetic bearing actuator design that allowed all of the above requirements be satisfied.

AXIAL MAGNETIC BEARING

One of the components influencing the system rotordynamics the most was the thrust disk needed to compensate 1750 lbf (7784 N) of axial loading. While the weight of the disk had essentially a fixed value for the given load, frequency of the first bending mode could be increased by locating this disk as close to the rotor center of mass as possible. In order to achieve this goal, an anisotropic axial magnetic bearing was developed to take advantage of the fact that higher axial load capacity was required in one direction than in the other: 1750 lbf towards the impeller, while only 750 lbf in the opposite direction. This fact suggested that a magnetic bearing with different pole areas on the opposite sides of the thrust disk could be designed and could use space available under the smaller pole to accommodate one of the mechanical back-up bearings. This arrangement is shown in Figure 1. Since power consumption was not a design driver, it was found advantageous to produce bias flux using bias coils rather than permanent magnets.

The force produced by the bearing is

$$F = \frac{1}{2\mu_0}\left(B_1^2 \cdot A_1 - B_2^2 \cdot A_2\right), \qquad (1)$$

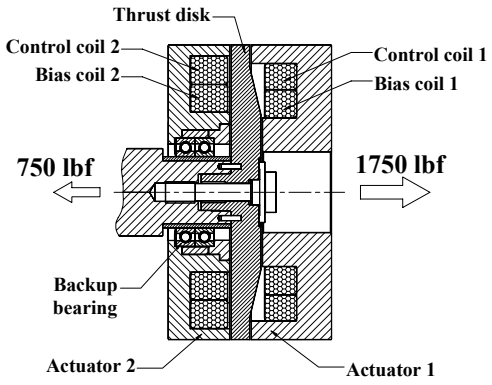

Figure 1. Asymmetric thrust magnetic bearing.

where B_1 and B_2 are the flux densities in the air gaps on the side of the bigger and smaller loadings respectively; A_1 and A_2 are the total pole surface areas, including inner and outer poles. The inner and outer pole areas are assumed to be equal.

Without loss of generality, we assign positive signs to both bias fields: $B_{b1} > 0$ and $B_{b2} > 0$. The total field in each actuator is found by superposition of the bias and control fields. Again, without loss of generality we assign a positive sign to the control field on the high load side when it is directed as the bias field. Then the equations for the total fields become:

$$B_1 = (B_{b1} + B_{c1}); \; B_2 = (B_{b2} - B_{c2}); \qquad (2)$$

Substituting (2) into (1) yields:

$$F = \frac{1}{2\mu_0}\begin{pmatrix}\left(B_{b1}^2 \cdot A_1 - B_{b2}^2 \cdot A_2\right) + \\ \left(B_{c1}^2 \cdot A_1 - B_{c2}^2 \cdot A_2\right) + \\ 2\left(B_{b1}B_{c1}A_1 + B_{b2}B_{c2}A_2\right)\end{pmatrix} \qquad (3)$$

The flux densities are assumed to be linear functions of the currents (no saturation occurs):

$$B_{b1} = \mu_0 \frac{N_{b1}I_{b1}}{2g}, \; B_{b2} = \mu_0 \frac{N_{b2}I_{b2}}{2g},$$

$$B_{c1} = \mu_0 \frac{N_{c1}I_{c1}}{2g}, \; B_{c2} = \mu_0 \frac{N_{c2}I_{c2}}{2g}, \qquad (4)$$

where N_{b1}, N_{b2} are numbers of turns in the bias coils, N_{c1}, N_{c2} are numbers of turns in the control coils, and g is the air gap between the actuator pole and the thrust disk.

We also assume that

$$I_{b1} = I_{b2} = I_b \text{ and } I_{c1} = I_{c2} = I_c. \qquad (5)$$

(coils are connected in series).

It can be observed then from the equation (3), that for the force to be a linear function of the control current, the following condition must be satisfied:

$$B_{c2}^2 A_2 = B_{c1}^2 A_1. \qquad (6)$$

Furthermore, for the force to be zero when the control current is zero, we need:

$$B_{b2}^2 A_2 = B_{b1}^2 A_1. \qquad (7)$$

Using (4) and (5), equations (6) and (7) can be rewritten as

$$\frac{N_{c1}^2}{N_{c2}^2} = \frac{A_2}{A_1} \text{ and } \frac{N_{b1}^2}{N_{b2}^2} = \frac{A_2}{A_1}. \qquad (8)$$

Equations (8) give the desired ratios between the pole surface areas and numbers of turns.

RADIAL MAGNETIC BEARINGS

While the radial magnetic bearings react much smaller loads (up to 175 lbf), their design is also important for the overall system performance. In order to minimize the bearing length and maximize the shaft diameter (both result in the increase of the first bending frequency), high magnetic saturation laminations (Carpenter Hiperco 50) were used as a material for the bearing actuator target.

The axial cross-section of the radial bearing is shown in Figure 2. The bearing is a variation of a patented homopolar, permanent magnet biased design used in a number of applications such as [1]. The bias flux in this bearing is generated by axially magnetized permanent magnets – a solution that results in a more compact and efficient design than when current-carrying coils are used for this purpose. The bias flux flow in the bearing axial plane is illustrated in Figure 3. Currents in the control coils produce magnetic flux in the radial plane of the laminated active pole and the laminated rotor part, which, when superimposed on the bias flux, result in radial force proportional to the control current.

Figure 4 clarifies the mechanism of generating radial force. In the upper pole, the control and bias flux sum up, while in the lower pole they subtract. Higher net flux density in the upper air gap results in the radial force acting in the positive Y direction.

An advantageous feature of this design is that the control flux does not flow through high reluctance permanent magnets. This minimizes size of the control coils as well as their power dissipation.

Bias flux density calculation

The electromagnetic analysis of the bias circuit is rather straightforward, and for the most part a reasonably accurate solution can be obtained analytically. A complication occurs, however, because of flux traveling normal to the lamination plane and

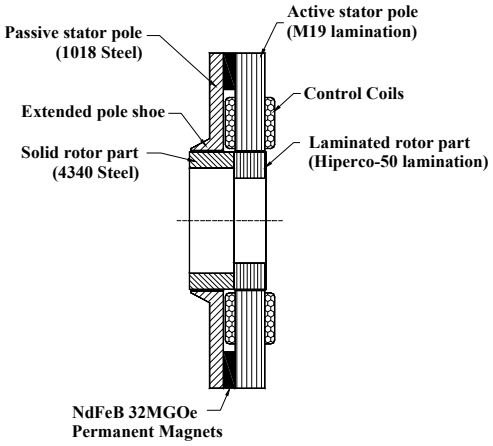

Figure 2. Axial cross-section of the radial bearing.

crossing high-reluctance insulation layers between the laminations. This results in a.) higher reluctance of the magnetic circuit than it would be if the pole were solid, and b.) non-uniform distribution of the magnetic flux density in the control air gap.

If there were no slots in the active pole, the problem could be attacked using a 2D FEA program that allows analysis of systems with rotational symmetry. The program called FEMM developed by Dr. D. Meeker [2] was found to be especially convenient. In contrast to most commercial FEA packages, FEMM does not require modeling each lamination and the insulation in between, but instead models the lamination stack as a continuous media with anisotropic magnetic properties.

The control pole slots eliminate the rotational symmetry and make this problem three dimensional. Nevertheless, it is possible to use 2D FEA if proper adjustments are made to take into account the slot effects.

As the first step, the representation of the laminated pole and control gaps in the 2D model are modified to make their reluctance match the reluctance of the 3D counterparts. This allows correct calculation of the magnet operating tangent and magnetic flux density in the rest of the system. Then bias flux density in the control air gap can be calculated.

It is easy to see that when the slots are present, the density of the magnetic flux crossing a cylinder of radius r located within the laminated pole and coaxial with the bearing axis is higher than if there were no slots by factor 1/ K_{pole}, where K_{pole} is the ratio of the area of the cylinder located in the iron to its total surface area. K_{pole} is referred to herein as the "pole factor" and, in general, can a function of r. Higher flux density B at each point implies higher magnetic strength H. For the reluctance of the laminated pole and control

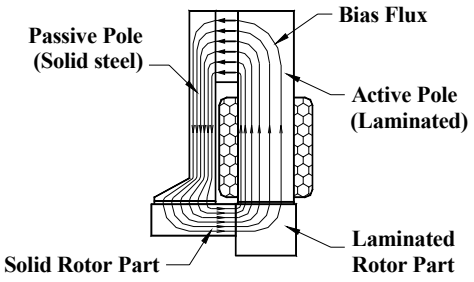

Figure 3. Bias Flux Flow.

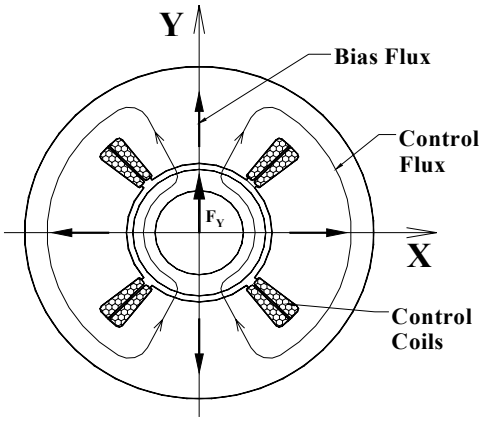

Figure 4. Generation of a radial force.

gap in the 2D model to match the reluctance of their 3D counterparts, the original B(H) curve is transformed into a B*(H*) curve of an equivalent media used in 2D model:

$$H^*(B^*, r) = H\left(B \cdot 1/K_{pole}(r)\right). \qquad (9)$$

This transformation assures that identical net fluxes entering laminated poles and air gaps in the original 3D system and its slotless 2D representation cause identical MMF drops.

The transformation (9) is very simple if the B(H) curve is linear. Thus for the control gap the original $B=\mu_0 H$ dependence after transformation (9) becomes $B^*=\mu_0 K_{pole0} \cdot H^*$, where K_{pole0} is the pole factor on the laminated pole ID.

It can also be noticed that the main part of the laminated pole reluctance is due to the insulation layers. Because of this, the B(H) curve within the lamination stack is also close to linear. To quantify how long the flux travels within the insulation compared to its path within the lamination, the stacking factor SF is introduced, defined as the ratio of the thickness of the lamination material in a stack vs total stack thickness. Assuming that reluctance of the lamination material is negligible, the effect of the winding slots can be taken

into account in a 2D model by redefining the stacking factor:

$$SF^*(r) = 1 - (1 - SF) / K_{pole}(r) \qquad (10)$$

Note that the equivalent stacking factor *SF** used in the model can be a function of the radius *r*. A practical way to reflect this dependence in the model is to split the representation of the slotted portion of the laminated pole radially into several cylindrical sections with different values of SF*.

Finally, after the FEA is complete, an inverse transformation obtains the bias flux density in the control air gap of the 3D system, B_{bias} :

$$B_{bias} = B^*_{bias} / K_{pole0}, \qquad (11)$$

where B^*_{bias} is the magnetic flux density calculated in the cylindrical air gap of the 2D FEA model.

Figure 5 shows flux distribution in the control air gap calculated using this technique and FEMM program (the curve is not scaled using (11)). The flux distribution is strongly non-uniform. The highest density occurs at the pole end closest to the magnet since the flux travels shortest distance across the lamination.

Negative stiffness calculation

One of the important parameters of the magnetic bearing actuator is the destabilizing negative stiffness exerted on the rotor due to the bias flux. High negative stiffness significantly complicates control design. The negative stiffness analysis would be a three dimensional problem even if we neglected winding slots, since it implies calculation of the force exerted on the rotor being displaced radially by some distance *e*. Presented is an approach that allows this calculation using 2D FEA. First, forces due to bias magnetic fields in the air gaps of the active and passive poles F_A and F_P are calculated separately and then the total force *F* is found as a sum

$$F = F_A + F_P \qquad (12)$$

Force due to the active pole bias field. Figure 6 shows one of the control poles. The pole length is given by the angle α; its orientation with respect to the displacement characterized by the angle *β*. Let the nominal value of the air gap be g_0. When the rotor is displaced from the central position, the air gap becomes a function of the polar angle *φ*:

$$g(\phi) = g_0 - e\cos\phi \qquad (13)$$

Let *U* be the MMF drop between the rotor surface and the poles. When the control pole is laminated, *U* is nearly the same in the circumferential direction for all poles, but may vary axially, i.e. *U* is a function of the axial coordinate *x*: *U=U(x)*.

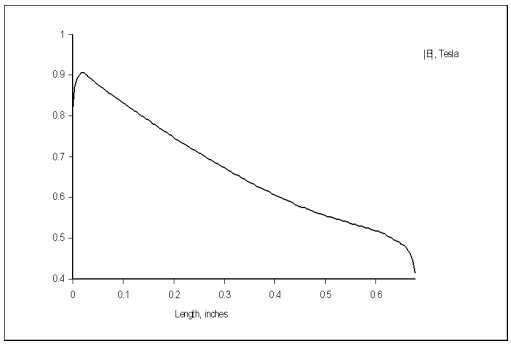

Figure 5. Axial distribution of the bias flux density in the control air gap.

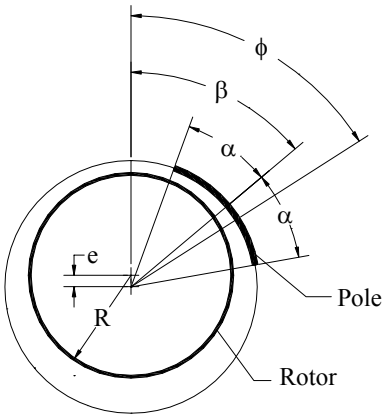

Figure 6: Geometry for the analysis of the negative radial stiffness due to the active pole.

The magnetic field strength in the air gap is then a function of both the polar angle and the axial coordinate:

$$H(\phi, x) = \frac{U(x)}{g(\phi)} = \frac{U(x)}{g_0 - e\cos(\phi)}. \qquad (14)$$

The magnetic flux density in the air gap is

$$B(\phi, x) = \mu_0 H(\phi, x) = \mu_0 \frac{U(x)}{g_0 - e\cos(\phi)} \qquad (15)$$

The magnetic flux through ONE pole per unit of the axial length is

$$\Phi_0(x) = \int_{\beta-\alpha}^{\beta+\alpha} B(\phi, x) R d\phi = \left(\mu_0 R \int_{\beta-\alpha}^{\beta+\alpha} \frac{1}{g_0 - e\cos(\phi)} d\phi \right) \cdot U(x) \qquad (16)$$

The integral in the brackets can be evaluated analytically. Then (16) becomes:

$$\Phi_0(x) = K_1 U(x) \qquad (17)$$

where

$$K_1 = \frac{2\mu_0 R}{\sqrt{g_0^2 - e^2}} \left\{ \begin{matrix} a\tan 2(X_1; Y_1) - \\ -a\tan 2\left(X_2; Y_2\right) \end{matrix} \right\};$$

$$X_1 = \sqrt{g_0^2 - e^2}\cos\left(\frac{\beta+\alpha}{2}\right);$$

$$Y_1 = (g_0 + e)\sin\left(\frac{\beta+\alpha}{2}\right);$$

$$X_2 = \sqrt{g_0^2 - e^2}\cos\left(\frac{\beta-\alpha}{2}\right);$$

$$Y_2 = (g_0 + e)\sin\left(\frac{\beta-\alpha}{2}\right). \qquad (18)$$

Note that *a*tan2 is an extension of the *a*tan function defined in all four quadrants (see for example [3]).

The total flux through ONE pole is

$$\Phi_1 = \int_0^L \Phi_0(x)dx = K_1 \int_0^L U(x)dx = K_1 U_{av} L_C,$$

where L_C is the axial length of the control pole and U_{av} is the average value of the MMF drop.

If all four poles are considered, the coefficients K_1 will be different for each pole, but $U(x)$ and, consequently, U_{av} will be the same.

The total flux through ALL FOUR poles will be

$$\Phi = \sum_{i=1}^{4} K_{1i} \times U_{av} L_C \qquad (19)$$

As a next step, the component of the force exerted by a control pole on the rotor against the displacement is calculated. This force per unit length is

$$f(x) = \frac{1}{2\mu_0}\int_{\beta-\alpha}^{\beta+\alpha} B(\phi, x)^2 R\cos(\phi)d\phi = \left(\frac{\mu_0 R}{2}\int_{\beta-\alpha}^{\beta+\alpha}\frac{\cos(\phi)}{\left(g_0 - e\cos(\phi)\right)^2}d\phi\right)U(x)^2 \qquad (20)$$

Again, the integral in bracket can be evaluated analytically, yielding

$$f(x) = K_2 U(x)^2, \qquad (21)$$

where

$$K_2 = \frac{\mu_0 R}{2}\left\{ \begin{matrix} \frac{g\sin(\beta+\alpha)}{(g^2 - e^2)(g - e\cos(\beta+\alpha))} - \\ -\frac{g\sin(\beta-\alpha)}{(g^2 - e^2)(g - e\cos(\beta+\alpha))} + \\ +\frac{1}{\mu_0 R}\frac{e}{g^2 - e^2}K_1 \end{matrix} \right\} \qquad (22)$$

The total force exerted on the rotor by the FOUR control poles is

$$F_C = \left(\sum_{i=1}^{4} K_{2i}\right)\int_0^L U^2(x)dx. \qquad (23)$$

The shape of the $U(x)$ (and consequently the shape of $B(x)$) is assumed not affected by the rotor displacement. The magnitude of $U(x)$, however, is affected by the displacement. To characterize the shape of $U(x)$, we introduce dimensionless $u(x)$:

$u(x) = U(x)/U_{av}$.

Note that U_{av} characterizes the magnitude (scaling factor) of $U(x)$. Using (19), U_{av} can be found as

$$U_{av} = \Phi \Big/ \left(L_C \sum_{i=1}^{4} K_{1i}\right). \qquad (24)$$

The shape function $u(x)$ can be obtained using the field distribution in the air gap, which was calculated earlier using FEA. Indeed, using (15) we can see that

$$u(x) = B(x)/B_{av}. \qquad (25)$$

Finally (23) is rewritten using definitions of U_{av} and $u(x)$ as

$$F_C = \frac{\sum_{i=1}^{4} K_{2i}}{\left(\sum_{i=1}^{4} K_{1i}\right)^2}\left(\frac{1}{L_c}\right)^2 \int_0^L u^2(x)dx \cdot \Phi^2 \qquad (26)$$

Equation (26) allows calculation of the radial force acting on the displaced rotor knowing the system geometry, rotor displacement, the axial bias flux Φ through all FOUR poles, and its axial distribution in the control gap $u(x)$. The latter two can be found using 2D FEA for the central rotor position. It can be noticed that the bias flux in this design does not change significantly when the rotor is displaced radially because the cross-section of the passive pole (Fig. 3) is chosen so that the pole is nearly saturated. The model, however, can be further refined to recalculate Φ for displaced rotor position.

Force due to the passive pole bias field. Similarly to how it was done for the active poles, it can be shown that the force exerted on the displaced rotor due to bias magnetic field in the air gap under the passive pole is

$$F_P = \frac{1}{2\mu_0}\frac{1}{2\pi R L_P}\frac{e}{\sqrt{g_0^2 - e^2}}\Phi^2, \qquad (27)$$

where L_P is the axial length of the passive pole.

It can be learned from (27) that F_P can be reduced by increasing the passive pole surface area $2\pi R L_P$. In our design it is realized through extending the pole axially as shown in Figure 3. The extended pole foot fits under end turns of the neighboring generator.

BEARING TEST RESULTS

The above described Gas Expander/Generator has been built and tested. Fig. 7 shows experimental and theoretical force vs current curves obtained with the above described asymmetric thrust bearing. The theoretical curve was calculated using FEMM.

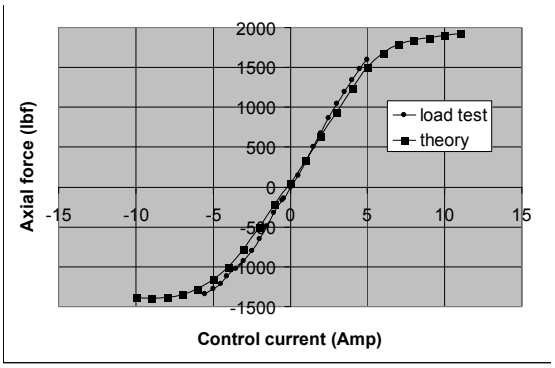

Figure 7. Theoretical and experimental axial force vs control current curves.

It can be observed that load capacities in different directions are different indeed, while the force vs current dependence remains linear until the actuator starts saturating.

The measured force vs current curve for the radial bearing is presented in Figure 8. In the linear range, the actuator gain was 29.9 lbf/A with the design value 29.7-32.9 lbf/A, depending on the lamination stacking factor and magnet energy product. These two are the primary uncertainties in the design process, which do not allow more accurate prediction of the bias flux and, consequently, the actuator gain and negative stiffness. The latter is especially sensitive to variations in the bias flux since it depends on its second power (see eq-s (26) and (27)). The expected values for the negative stiffness were in the range 10.6-13.0 ksi/in. Figure 9 shows the measured radial destabilizing force vs displacement curve. This curve implies negative stiffness of 10.2 ksi/in.

In order to validate the method of calculating negative stiffness, a more accurate estimate of the bias flux was needed. As mentioned earlier, the latter was significantly influenced by the lamination stacking factor and magnet energy product, which could not be accurately measured in this unit. To eliminate these from the analysis, the flux was estimated using measured actuator gain: 29.9 lbf/A. This produced the flux estimate of 3.51mWb. Using this value and equations (12), (26) and (27), the negative stiffness was estimated as 10.7 ksi/in – less than 5% error.

CONCLUSION

The magnetic bearing system that was developed, built and tested features several novel technical solutions including an anisotropic axial bearing and homopolar PM-biased high-efficiency radial magnetic bearings.

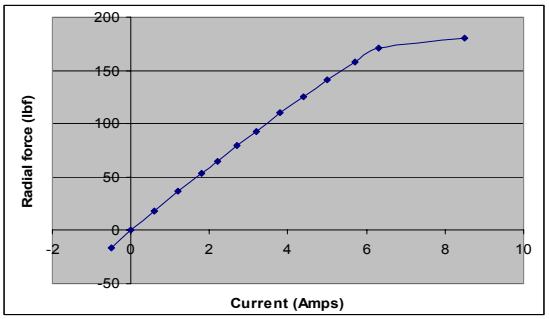

Figure 8. Measured radial force vs control current curve.

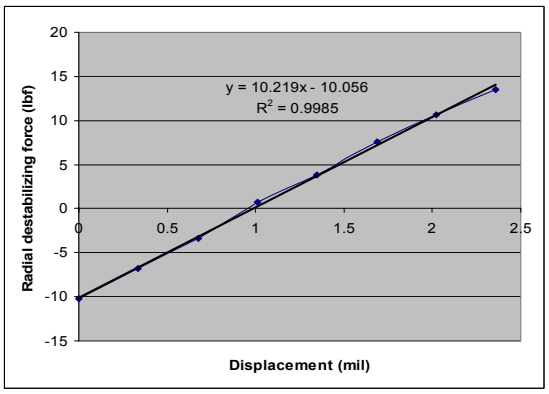

Figure 9. Measured radial destabilizing force vs displacement curve.

The axial magnetic bearing has different pole areas on the opposite sides of the thrust disk, which simplifies its integration into the system. Regardless of this fact, it offers linear force vs control current dependence, which significantly simplifies the control algorithm.

Presented analysis methods allow accurate calculation of the bias flux density and negative stiffness in homopolar radial bearing using 2D FEA, in spite of the three-dimensional nature of the problem. The analysis results are found in good agreement with experimental data.

REFERENCES

1. Hawkins, L., Blumber, E., Paylan, A., "Development of an Energy Storage Flywheel for Industrial Applications", Proc. of 7th Intl. Symposium on Magnetic Suspension Technology, Fukuoka, Japan, 2003.
2. http://femm.foster-miller.com/
3. MatLAB manual (MathWorks Inc.)